Applied Mathematical Modelling 40 (2016) 1959–1971

Contents lists available at ScienceDirect

Applied Mathematical Modelling

journal homepage: www.elsevier.com/locate/apm

Solution of an industrially relevant coupled magneto–mechanical problem set on an axisymmetric domain

Paul David Ledger[a,*], Antonio J. Gil[a], Roman Poya[a], Marcel Kruip[b], Ian Wilkinson[b], Scott Bagwell[a]

[a] Zienkiewicz Centre for Computational Engineering, College of Engineering, Swansea University Bay Campus, Crymlyn Burrows, Swansea SA1 8EN, UK
[b] Siemens plc, Healthcare Sector, MR Magnet Technology, Wharf Road, Eynsham, Witney, Oxon OX29 4BP, UK

ARTICLE INFO

Article history:
Received 19 December 2014
Revised 26 May 2015
Accepted 25 September 2015
Available online 5 October 2015

Keywords:
Magneto–mechanical coupling
hp-finite elements
Axisymmetric geometry
MRI scanners

ABSTRACT

Eddy currents are generated when low frequency magnetic fields interact with conducting components and this, in turn, generates Lorentz forces, which can cause these metallic components to deform and vibrate. An important application of this magneto–mechanical coupling is in coil design for magnetic resonance imaging scanners, where such vibrations can have unwanted effects such as ghosting of images, reduction of the life span of devices and discomfort for the patient. This work is aimed at developing an accurate computational tool for better understanding these deformations by considering a benchmark problem proposed by Siemens plc (Kruip, *personal communication*, 2013) on an idealised axisymmetric geometry. We present a new fixed point algorithm and develop new weak variational statements, which use a stress tensor approach for force calculation and permit discretisation using H^1 conforming *hp*-version finite elements. Numerical results are included, which show the importance of high order finite elements for predicting the eddy currents and the associated coupling in the resonance region.

1. Introduction

Magnetic resonance imaging (MRI) scanners essentially consist of a main magnet, which produces a strong uniform magnetic field across the bore cross-section and a second set of gradient coils, which produce pulsed field gradients in order to generate an image. The *X*-, *Y*-, and *Z*-gradient coils produce gradients fields in the appropriate specified direction and, by activating combinations of these coils, gradient fields can be generated in any specified direction [1]. The main magnet is the largest and most expensive part of an MRI scanner. Three types of magnet could be used. A first option would consist of a permanent magnet made from ferromagnetic materials. A second option would be a resistive magnet consisting of a solenoid made from wound copper wire, whilst the third option would be a superconducting magnet, typically cooled by liquid helium. Permanent magnets are expensive and bulky, difficult to install and have issues as they cannot be turned off. Resistive magnets are cheaper, but their

* Corresponding author. Tel.: +44 1792 602554.
E-mail addresses: P.D.Ledger@swansea.ac.uk (P.D. Ledger), A.J.Gil@swansea.ac.uk (A.J. Gil), r.poya@swansea.ac.uk (R. Poya), 638988@swansea.ac.uk (S. Bagwell).
URL: http://www.swansea.ac.uk/staff/academic/engineering/ledgerpaul/ (P.D. Ledger)

http://dx.doi.org/10.1016/j.apm.2015.09.030
S0307-904X(15)00564-8/

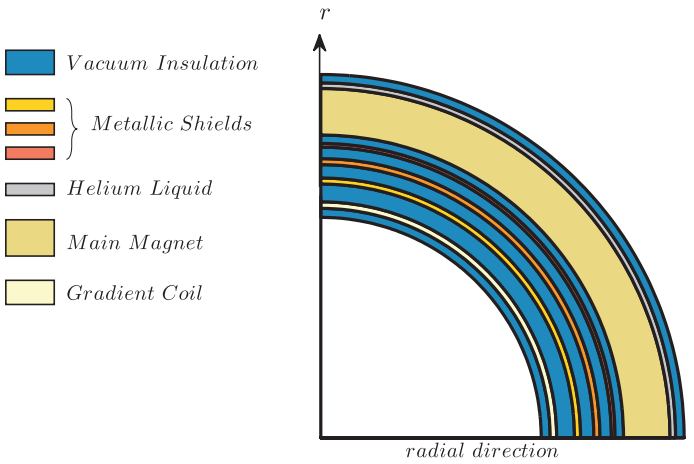

Fig. 1. Radial cross-section of a simple MRI scanner.

field strength and stability are limited. Superconducting electro-magnets allow for very high fields strengths, are very stable and, therefore, despite their high construction costs, they remain the most common type of magnet found in MRI scanners today.

The superconducting magnet consists of coils of superconducting wire immersed in liquid helium contained within a vessel called the cryostat. The cryostat itself consists of a series of metallic shields and the outer vacuum container, as shown in Fig. 1. Being metallic, the shields and outer vacuum container can support eddy currents in the presence of changing magnetic fields. These eddy currents can cause the magnetic field to perturb. In addition, eddy currents give rise to Lorentz forces, which exert magneto–mechanical stresses on the conducting components and cause them to deform and vibrate. Changes in the geometry of the conductors cause further perturbations in the magnetic field and further eddy currents are thus developed.

Mechanical vibrations and deformations are undesirable in MRI scanners for several reasons. Firstly, they can lead to undesired artefacts and ghosting in medical images, which can potentially cause problems in medical diagnosis. Secondly, the vibrations can cause noise which can be disconcerting for the patient whilst inside the MRI scanner and, thirdly, they can reduce the life span of the device. Thus, in order to improve the design of the main magnet, there exists a strong motivation to be able to quantify the mechanical vibrations and deformations generated within the magnet and the surrounding cryostat.

Computational simulation offers great promise for this, as it enables different designs to be tested in a virtual environment in an efficient manner with low risk. Indeed the coupled simulation of magneto–mechanical problems is a very hot topic with a large number of articles recently been published in journals and international conferences e.g. [2–9] as a small sample. Commercial finite element packages are now widely available for the single field solution of mechanical and electromagnetic problems in isolation. More recently, commercial packages for the solution of coupled electro–magneto–mechanical problems, such as ANSYS [10], COMSOL Multiphysics [11] and Numerical analysis of Coupled Systems (NACS) [12], have become available. Nevertheless, the challenging nature of some industrial problems often means that commercial software requires additional customised routines to be capable of aiding in the design process. This is certainly the case when considering the analysis of the coupled effects in MRI scanners, since unless careful consideration is given to the coupling mechanisms involved, the software will be incapable of delivering accurate results in an industrially relevant turnaround time.

In the context of magneto–mechanical coupling in MRI scanners, Rausch et al. [5] proposed a temporal solution algorithm using low order finite elements, which was later extended to also include acoustic effects [6]. More recently, the mechanical vibrations for ultra high frequency MRI scanners have been investigated [9] and a modal analysis has been presented, which is quoted to give a 20–100 factor reduction in computational time compared to a transient computation [8]. An important aspect of the simulation of magneto–mechanical problems is the calculation of the forces exerted on the mechanical body, due to the presence of magnetic fields. Typically, a local force calculation is required and common approaches include obtaining local forces by evaluating the divergence of a stress tensor or using the virtual work principle. These approaches have been reviewed in [13]. The evaluation of local forces using the electromotive stress tensor tends not to be pursued since the application of the divergence operator can lead to loss in accuracy (e.g. in the context of fluid structure interaction [14–16]). For further details on the virtual work approach we refer to [17]. In the context of problems in electrostriction and magnetostriction in solids and fluids we have adopted an alternative approach for the calculation of electro– magneto–mechanical forces [18,19], which recalls that the electromotive force can instead be expressed as the divergence of a stress tensor plus the addition of a momentum term [20,21]. However, our approach has an important and subtle difference. Rather than first evaluating the local force, from the divergence of the stress tensor, and then applying this as a nodal force in the mechanical problem, we instead work directly with the electromotive stress tensor and by-pass the need to calculate local forces, thereby avoiding the associated loss of accuracy. Such an approach allows for natural calculation of stresses resulting from the presence of electromagnetic fields and fits naturally into the finite element framework.

We investigate a benchmark problem proposed by Siemens plc based on an experiment, which they have recently conducted. The experiment consists of the main components of the cryostat for a simplified rotational symmetric geometry. Despite its

simplifications, it bears considerable similarity to the geometries used in previous simulations of magneto–mechanical responses from MRI scanners [5,6] and therefore provides an extremely useful benchmark. In order to ensure the small skin depths are well-resolved across a range of frequencies, we employ an *hp* finite element approach, which allows for the possibility of using arbitrary high element order as well as local mesh refinements (e.g. [22–25] and references therein). Although the work of Rausch et al. [5,6] has already considered a full three dimensional MRI geometry, we feel there is still considerable scope for considering the axisymmetric case in order to ensure that fields are correctly resolved, eddy current layers are accurately predicted and that the resulting magneto–mechanical coupling gives an accurate prediction of resonance behaviour.

The novel contributions of this work are as follows: first, rather than the moving mesh and direct force calculation strategy previously employed in [5,6], we adopt a stress tensor approach, similar to that described in [18,19], which by-passes the need to calculate local forces and provides a natural framework for the coupling. Second, inspired by the work of Lacoste [26], we provide a rigorous treatment of the weak forms of the coupled eddy current and linear elastic problems in axisymmetric coordinates, which allows us to overcome frequently adopted approximations at the radial axis e.g. [27–30]. Furthermore, in these new weak variational statements, we adopt an *hp*–finite element discretisation, ensuring accurate mechanical and electromagnetic field computation, which is important for resolving the fields in the thin skin depths of the conductors and resolve the nonlinearity by applying a fixed point algorithm.

The paper is organised as follows: in Section 2 we introduce some mathematical notation that will be employed throughout the paper and present the set of governing equations. In Section 3 we describe the industrial model problem and a series of simplifying assumptions, which allow the problem to be solved in the frequency domain. We describe our computational treatment of axisymmetric domains in Section 4 and present a series of numerical results in Section 5. We close with concluding remarks in Section 6.

2. Governing equations

Throughout the paper, the symbol $(\cdot)$ is used to indicate the scalar product or contraction of a single index $\boldsymbol{a}\cdot\boldsymbol{b}=a_ib_i$; the symbol $(:)$ is used to indicate double contraction of two indices $\boldsymbol{A}:\boldsymbol{B}=A_{ij}B_{ij}$; the symbol $(\times)$ is used to indicate the cross product $[\boldsymbol{a}\times\boldsymbol{b}]_i=\varepsilon_{ijk}a_jb_k$ via the third order permutation tensor ε_{ijk} and the symbol $(\otimes)$ is used to indicate the outer or dyadic product $[\boldsymbol{a}\otimes\boldsymbol{b}]_{ij}=a_ib_j$.

In order to describe small deformations of conducting elastic bodies, due to the presence of electromagnetic forces exerted in an electro–magneto–mechanical system, the coupled set of time-dependent Maxwell equations

$$\nabla\times\mathcal{H}=\mathcal{J}+\frac{\partial\mathcal{D}}{\partial t}=\mathcal{J}^s+\underline{\boldsymbol{\gamma}\left(\frac{\partial\mathcal{U}}{\partial t}\times\mathcal{B}\right)}+\mathcal{J}^o+\frac{\partial\mathcal{D}}{\partial t}, \tag{1a}$$

$$\nabla\times\mathcal{E}=-\frac{\partial\mathcal{B}}{\partial t}, \tag{1b}$$

$$\nabla\cdot\mathcal{B}=0, \tag{1c}$$

$$\nabla\cdot\mathcal{D}=\rho^e, \tag{1d}$$

and elasticity equation

$$\nabla\cdot\boldsymbol{\sigma}^m(\mathcal{U})+\boldsymbol{b}(\mathcal{E},\mathcal{H})=\nabla\cdot\boldsymbol{\sigma}^m(\mathcal{U})+\underline{\rho^e\mathcal{E}+\mathcal{J}\times\mathcal{B}}=\rho\frac{\partial^2\mathcal{U}}{\partial t^2}, \tag{2}$$

must be solved e.g. [17]. In the above, calligraphic symbols are used to denote time dependent quantities, $\mathcal{E}(t)$ is the electric field vector, $\mathcal{H}(t)$ is the magnetic field vector, $\mathcal{B}(t)$ is the magnetic flux density vector, $\mathcal{D}(t)$ is the electric displacement, and $\mathcal{U}(t)$ is the mechanical displacement, all of which are time-dependent. In addition, $\partial\mathcal{D}/\partial t$ is the displacement current, $\mathcal{J}^s(t)$ is the applied current from the coil, $\mathcal{J}^o(t)$ is the Ohmic or eddy current, ρ^e is the volume charge density, and the electromagnetic constitutive relations are

$$\mathcal{J}^o:=\boldsymbol{\gamma}\mathcal{E},\quad \mathcal{D}:=\boldsymbol{\epsilon}\mathcal{E},\quad \mathcal{B}:=\boldsymbol{\mu}\mathcal{H}, \tag{3}$$

where $\boldsymbol{\gamma}$ is electric conductivity tensor, $\boldsymbol{\epsilon}$ is dielectric permittivity tensor, and $\boldsymbol{\mu}$ is electromagnetic permeability tensor. In the elasticity equation, ρ denotes the mass density

$$\boldsymbol{\sigma}^m(\mathcal{U}):=\lambda\mathrm{tr}(\boldsymbol{\varepsilon}(\mathcal{U}))\boldsymbol{I}+2G\boldsymbol{\varepsilon}(\mathcal{U}), \tag{4}$$

is the Cauchy stress tensor, λ, G are the Lamé parameters, $\boldsymbol{\varepsilon}(\mathcal{U}):=\frac{1}{2}(\nabla\mathcal{U}+(\nabla\mathcal{U})^T)$ is the linearised strain tensor and $\boldsymbol{I}$ is the identity tensor. The underlined terms in (1) and (2) reveal the challenging nature of the coupling, since the highlighted Lorentz current depends on $\mathcal{U}$, which itself, through the highlighted body force, depends nonlinearly on $\mathcal{J}$. Thus, we see that (1)–(4) form a highly nonlinear system of partial differential equations in $\mathcal{E}$, $\mathcal{H}$, and $\mathcal{U}$.

3. The industrial problem and simplifying assumptions

In the context of developing a better understanding of the deformations caused by the presence of eddy currents in the conducting components of the cryostat, an appropriately scaled experiment was proposed by Siemens Magnet Technology, Siemens plc [31]. This experiment consists of a simplified and idealised geometry consisting only of the *Z*-gradient coil, the main coil, the stainless steel oxygen vacuum chamber (OVC), and aluminium alloy 77K and 4K shields, the latter shields and OVC being modelled as solid cylinders. The actual dimensions and material parameters cannot be stated in order to maintain the company's competitive advantage. We remark that a similar setup has been employed in [5,6] for the simulations of magneto–mechanical vibrations from MRI scanners. But, (the confidential) actual measurement data for the geometry considered here does allow us to further verify our model.

3.1. Simplifying assumptions

We now briefly summarise the main key assumptions made in the model, which, in part, have similarities to earlier work [4–6,8], but are nonetheless recalled here in order to provide a rigorous justification for each stage of the model.

3.1.1. Constitutive behaviour of materials

In addition to assuming that the materials will each behave elastically, we choose to neglect *strictive* effects, which cause the material's permittivity and permeability to change under the influence of mechanical strains (or fluid strain rates). Instead, we consider homogeneous isotropic materials such that $\boldsymbol{\epsilon} = \epsilon \boldsymbol{I}$, $\boldsymbol{\mu} = \mu \boldsymbol{I}$, and $\boldsymbol{\gamma} = \gamma \boldsymbol{I}$, where ϵ, μ, and γ are assumed constant for each material and $\rho^e = 0$.

3.1.2. Coils

The gradient and main coils are assumed to carry volume current densities with uniform amplitudes, neglecting inductance effects. Furthermore, the *Z*-gradient coils are assumed to be supplied with a harmonic time varying current source rather than pulsed currents, as they would be in an actual scanner. This means that the current source $\mathcal{J}^s$ is comprised of two parts (with different supports), such that,

$$\mathcal{J}^s(t) = \boldsymbol{J}^s_{DC} + \mathcal{J}^s_{AC}(t), \tag{5}$$

where $\boldsymbol{J}^s_{DC}$ is the static (time-independent) divergence free volume current density associated with the main coils and $\mathcal{J}^s_{AC}(t)$ is the sinusoidal time varying divergence free current density associated with the *Z*-gradient coils.

3.1.3. Eddy current approximation

The free space region has been truncated a finite distance away from the conductor on the basis that the eddy current approximation applies, due to the high conductivity of the conducting components and the (relatively) low frequencies of operation that will be considered [32]. This means that wave propagation effects will be ignored by neglecting the displacement currents $\frac{\partial \mathcal{D}}{\partial t}$ in (1) and reduces the electro–magneto–mechanical problem in (1)–(4) to a magneto–mechanical coupled problem. Furthermore, for the eddy current model, the electromagnetic fields decay away from the coils and conducting components according to [33]

$$\mathcal{E} = O\left(\frac{1}{|\boldsymbol{x}|}\right), \quad \mathcal{H} = O\left(\frac{1}{|\boldsymbol{x}|}\right) \quad \text{as } |\boldsymbol{x}| \to \infty,$$

which, in turn, allows us to truncate the domain a finite distance away from the conducting components and coils and apply, as an approximation, zero tangential conditions on the fields at the outer boundary.

3.1.4. Stress tensor formulation

In a departure from [4–6,8], and following [21], we note that $\boldsymbol{b}$ can be written as the divergence of a stress tensor plus a momentum term $\frac{\partial}{\partial t}(\mathcal{D} \times \mathcal{B})$. On the basis of the constitutive behaviour of the materials, this simplifies to

$$\boldsymbol{b}(\mathcal{E}, \mathcal{H}) = \nabla \cdot \boldsymbol{\sigma}^e(\mu, \mathcal{H}) + \nabla \cdot \boldsymbol{\sigma}^e(\epsilon, \mathcal{E}) + \frac{\partial}{\partial t}(\mathcal{D} \times \mathcal{B}) \approx \nabla \cdot \boldsymbol{\sigma}^e(\mu, \mathcal{H}), \tag{6a}$$

$$\boldsymbol{\sigma}^e(\mu, \mathcal{H}) = \mu\left(\mathcal{H} \otimes \mathcal{H} - \frac{1}{2}(\mathcal{H} \cdot \mathcal{H})\boldsymbol{I}\right), \tag{6b}$$

where the terms $\nabla \cdot \boldsymbol{\sigma}^e(\epsilon, \mathcal{E}) + \frac{\partial}{\partial t}(\mathcal{D} \times \mathcal{B})$ have been neglected in order to be consistent with the aforementioned approaches and the eddy current approximation. We assume them to be approximately zero for the materials under consideration, which, in turn, means that we will not be required to explicitly evaluate $\boldsymbol{b}$.

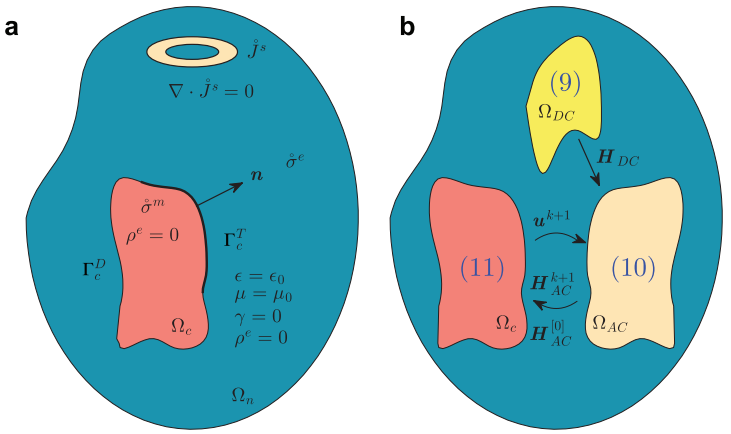

Fig. 2. Geometrical description of coupled magneto–mechanical model: (a) a fully coupled problem and (b) algorithmic idealisation.

3.2. Time dependent mathematical model

For future reference, we set $\Omega = \Omega_n \cup \Omega_c \subset \mathbb{R}^3$ where Ω_n is a suitably truncated region of free space (where $\epsilon = \epsilon_0 \approx 8.854 \times 10^{-12}$F/m, $\mu = \mu_0 = 4\pi \times 10^{-7}$H/m and $\gamma = 0$S/m) and $\Omega_c = \Omega_c^{4K} \cup \Omega_c^{77K} \cup \Omega_c^{OVC}$ denotes the conducting components.

On consideration of the assumptions made above, the time-dependent model for coupled magneto–mechanical problems can be stated as: Find $(\mathcal{E}, \mathcal{H}, \mathcal{U}) \in (\mathbb{R}^3 \times [0, \mathcal{T}])^3$ such that

$$\nabla \times \mathcal{H} = \mathcal{J}^s + \gamma\mu\left(\frac{\partial \mathcal{U}}{\partial t} \times \mathcal{H}\right) + \gamma\mathcal{E} \quad \text{in } \Omega, \tag{7a}$$

$$\nabla \times \mathcal{E} = -\frac{\partial(\mu\mathcal{H})}{\partial t} \quad \text{in } \Omega, \tag{7b}$$

$$\nabla \cdot (\mu\mathcal{H}) = \nabla \cdot (\epsilon\mathcal{E}) = \nabla \cdot \mathcal{J} = \nabla \cdot \mathcal{J}^s = 0 \quad \text{in } \Omega, \tag{7c}$$

$$\nabla \cdot (\boldsymbol{\sigma}^m(\mathcal{U}) + \boldsymbol{\sigma}^e(\mu, \mathcal{H})) = \rho\frac{\partial^2 \mathcal{U}}{\partial t^2} \quad \text{in } \Omega_c, \tag{7d}$$

$$\boldsymbol{\sigma}^m(\mathcal{U}) = \lambda \mathrm{tr}(\boldsymbol{\varepsilon}(\mathcal{U}))\boldsymbol{I} + 2G\boldsymbol{\varepsilon}(\mathcal{U}) \quad \text{in } \Omega_c, \tag{7e}$$

$$\boldsymbol{\sigma}^e(\mu, \mathcal{H}) = \mu\left(\mathcal{H} \otimes \mathcal{H} - \frac{1}{2}(\mathcal{H} \cdot \mathcal{H})\boldsymbol{I}\right) \quad \text{in } \Omega_c, \tag{7f}$$

$$\mathcal{H}(t = 0) = \mathcal{H}_0, \ \mathcal{E}(t = 0) = \mathcal{E}_0 \quad \text{in } \Omega, \tag{7g}$$

$$\mathcal{U}(t = 0) = \mathcal{U}_0 \quad \text{in } \Omega_c, \tag{7h}$$

$$\boldsymbol{n} \times \mathcal{E} = \boldsymbol{0}, \ \boldsymbol{n} \times \mathcal{H} = \boldsymbol{0} \quad \text{on } \partial\Omega, \tag{7i}$$

$$\mathcal{U} = \mathcal{U}_D \quad \text{on } \Gamma_c^D \tag{7j}$$

$$(\boldsymbol{\sigma}^m(\mathcal{U}) + \boldsymbol{\sigma}^e(\mu, \mathcal{H}))\boldsymbol{n} = \boldsymbol{t} \quad \text{on } \Gamma_c^T, \tag{7k}$$

where initial and boundary conditions must be supplied for the fields. We set $\mathcal{U}_D = \boldsymbol{0}$ on Γ_c^D in order to fix the shields in space and have that $\partial\Omega_c := \Gamma_c^D \cup \Gamma_c^T$. In addition, appropriate interface conditions should be supplied for each of the fields in a similar manner to [18]. Computational approaches to the solution of this equation system in three dimensions, using low-order finite elements, have been presented in [3,5,7,17].

3.3. Simplified time-harmonic model

From a design point of view, one would like to solve the coupled system (7) in the frequency rather than the time domain (Fig. 2). This is because the former is better placed to give the computational speed that engineers and physicists require in order to ensure the fast turnaround of computational results and keep costs to a minimum. Moreover, in principle, this is better suited to sweep quickly over input frequencies for the *Z*-gradient coil and obtain the dissipated power as a function of this input.

In the conference presentation [8] a time harmonic model for analysis of (7) has been presented, where the body force is not expressed as the divergence of a stress tensor. We remark that a naive introduction of the complex amplitudes $(\boldsymbol{E}, \boldsymbol{H}, \boldsymbol{J}, \boldsymbol{u}) \in ((\mathbb{C})^3)^4$ and setting

$$\mathcal{E} = \mathrm{Re}(\boldsymbol{E}e^{\mathrm{i}\omega t}), \quad \mathcal{J}^s = \mathrm{Re}(\boldsymbol{J}^s e^{\mathrm{i}\omega t}),$$
$$\mathcal{H} = \mathrm{Re}(\boldsymbol{H}e^{\mathrm{i}\omega t}), \quad \mathcal{U} = \mathrm{Re}(\boldsymbol{u}e^{\mathrm{i}\omega t}),$$

fails for the following reasons. Firstly, recalling (5), prevents us from representing $\mathcal{J}^s$ in terms of a complex amplitude vector $\boldsymbol{J}^s$ and a complex phasor with a single frequency ω. Secondly, the cross product term in (7a) yields a complex phasor $e^{2\mathrm{i}\omega t}$ that does not cancel with $e^{\mathrm{i}\omega t}$ associated with the other terms. Thirdly, and similarly, the quadratic terms in $\mathcal{H}$ in (7g) yields a complex phasor $e^{2\mathrm{i}\omega t}$ that does not cancel with the other terms in (7e).

The approach pursued in [8] is based on the ansatz

$$\mathcal{H}(t) \approx \boldsymbol{H}_{DC} + \mathrm{Re}(\boldsymbol{H}_{AC}e^{\mathrm{i}\omega t}), \tag{8}$$

and neglecting terms involving products of temporal derivatives in (7), where $\boldsymbol{b}$ is not expressed in stress tensor form. These are naturally approximations, which neglect non-linearity in the system. In the following, we state fully the boundary value problems for $\boldsymbol{H}_{DC}$ and $\boldsymbol{H}_{AC}$ implied by [8] and present a new stress–tensor approach for handling $\boldsymbol{b}$.

3.3.1. Electromagnetic fields associated with the DC coil

In the absence of the Z-gradient coils and conducting components, the main coil, with volume current density $\boldsymbol{J}^s_{DC}$, generates a static magnetic field. Let Ω_{DC} be the configuration of Ω in which the components of Ω_c are treated as free space, then, the resulting static magnetic field $\boldsymbol{H}_{DC}$ is associated with the solution of the problem: Find $\boldsymbol{A}_{DC} \in \mathbb{R}^3$ such that

$$\nabla \times \mu_0^{-1} \nabla \times \boldsymbol{A}_{DC} = \boldsymbol{J}^s_{DC} \quad \text{in } \Omega_{DC}, \tag{9a}$$

$$\nabla \cdot \boldsymbol{A}_{DC} = 0 \quad \text{in } \Omega_{DC}, \tag{9b}$$

$$\boldsymbol{n} \times \boldsymbol{A}_{DC} = \boldsymbol{0} \quad \text{on } \partial\Omega_{DC}, \tag{9c}$$

where $\boldsymbol{B}_{DC} := \mu_0 \boldsymbol{H}_{DC} = \nabla \times \boldsymbol{A}_{DC}$. In the above, $\boldsymbol{A}_{DC}$ is a static magnetic vector potential, the Coulomb gauge (9b) is used to ensure uniqueness of the solution (e.g. [25]) and the far field boundary condition follows from the previous approximation of the far field decay of the fields used in (7).

3.3.2. Electromagnetic fields associated with the AC coil

In the absence of the main coils, but in presence of the conducting components, the (AC) Z-gradient coils generate a time dependent magnetic field. Introducing a simplification of the Lorentz current, which depends on a time harmonic displacement $\boldsymbol{u} \in \mathbb{C}^3$ of the conducting components in Ω_c and the static $\boldsymbol{H}_{DC} \in \mathbb{R}^3$, the time harmonic problem is introduced as: Find $\boldsymbol{A}_{AC}(\boldsymbol{u}) \in \mathbb{C}^3$ such that

$$\nabla \times \mu^{-1} \nabla \times \boldsymbol{A}_{AC} + \mathrm{i}\omega\gamma \boldsymbol{A}_{AC} = \gamma \mathrm{i}\omega\mu \boldsymbol{u} \times \boldsymbol{H}_{DC} \quad \text{in } \Omega_c, \tag{10a}$$

$$\nabla \times \mu_0^{-1} \nabla \times \boldsymbol{A}_{AC} = \boldsymbol{J}^s_{AC} \quad \text{in } \Omega_n, \tag{10b}$$

$$\nabla \cdot \boldsymbol{A}_{AC} = 0 \quad \text{in } \Omega_n, \tag{10c}$$

$$\boldsymbol{n} \times \boldsymbol{A}_{AC} = \boldsymbol{0} \quad \text{on } \partial\Omega_n, \tag{10d}$$

where $\boldsymbol{B}_{AC} := \mu \boldsymbol{H}_{AC} = \nabla \times \boldsymbol{A}_{AC}$ and the Coulomb gauge as well as the approximate far field conditions have been applied in a similar manner to (9).

3.3.3. Mechanical displacement field associated with conductors

Next, we introduce our new time-harmonic formulation of the mechanical problem as follows: Find $\boldsymbol{u}(\boldsymbol{H}_{DC}, \boldsymbol{H}_{AC}) \in \mathbb{C}^3$ such that

$$\nabla \cdot (\boldsymbol{\sigma}^m(\boldsymbol{u}) + \boldsymbol{T}(\boldsymbol{H}_{DC}, \boldsymbol{H}_{AC})) = -\rho\omega^2 \boldsymbol{u} \quad \text{in } \Omega_c, \tag{11a}$$

$$\boldsymbol{u} = \boldsymbol{u^D} \quad \text{on } \Gamma_c^D, \tag{11b}$$

$$(\boldsymbol{\sigma}^m(\boldsymbol{u}) + \boldsymbol{T}(\boldsymbol{H_{DC}}, \boldsymbol{H_{AC}})\boldsymbol{n} = \boldsymbol{t} \quad \text{on } \Gamma_c^N, \tag{11c}$$

where $\partial\Omega_c = \Gamma_c^D \cup \Gamma_c^N$, $\boldsymbol{\sigma}^e(\mu, \mathcal{H}) \approx \mathrm{Re}(\boldsymbol{T}e^{\mathrm{i}\omega t})$ and $\boldsymbol{T} = \boldsymbol{T}^c - \mathrm{i}\boldsymbol{T}^s = \mathrm{Re}(\boldsymbol{T}) + \mathrm{iIm}(\boldsymbol{T})$ with

$$\boldsymbol{T}^c = \mu(\boldsymbol{H}_{DC} \otimes \boldsymbol{H}^c_{AC} + \boldsymbol{H}^c_{AC} \otimes \boldsymbol{H}_{DC} - \boldsymbol{H}_{DC} \cdot \boldsymbol{H}^c_{AC}\boldsymbol{I}), \tag{12a}$$

$$\boldsymbol{T}^s = \mu(\boldsymbol{H}_{DC} \otimes \boldsymbol{H}^s_{AC} + \boldsymbol{H}^s_{AC} \otimes \boldsymbol{H}_{DC} - \boldsymbol{H}_{DC} \cdot \boldsymbol{H}^s_{AC}\boldsymbol{I}), \tag{12b}$$

and $\boldsymbol{H}_{AC} = \boldsymbol{H}^c_{AC} - \mathrm{i}\boldsymbol{H}^s_{AC} = \mathrm{Re}(\boldsymbol{H}_{AC}) + \mathrm{iIm}(\boldsymbol{H}_{AC})$. This result stems from the ansatz (8), the formula (6b) and gathering only those terms associated with frequency ω.

In reality, the application of the ansatz will lead to the additional term stress tensors $\boldsymbol{T}_0$ and $\boldsymbol{T}_2 = \boldsymbol{T}^c_2 - \mathrm{i}\boldsymbol{T}^s_2 = \mathrm{Re}(\boldsymbol{T}_2) + \mathrm{iIm}(\boldsymbol{T}_2)$, which are associated with a static mechanical problem and a time harmonic mechanical problem with phasor $e^{2\mathrm{i}\omega t}$, respectively, where

$$\boldsymbol{T}_0 = \mu\left(\boldsymbol{H}_{DC}\otimes\boldsymbol{H}_{DC} + \frac{1}{2}\boldsymbol{H}^c_{AC}\otimes\boldsymbol{H}^c_{AC} + \frac{1}{2}\boldsymbol{H}^s_{AC}\otimes\boldsymbol{H}^s_{AC} - \frac{1}{2}\left(\boldsymbol{H}_{DC}\cdot\boldsymbol{H}_{DC} + \frac{1}{2}\boldsymbol{H}^c_{AC}\cdot\boldsymbol{H}^c_{AC} + \frac{1}{2}\boldsymbol{H}^s_{AC}\cdot\boldsymbol{H}^s_{AC}\right)\boldsymbol{I}\right), \tag{13}$$

$$\boldsymbol{T}^c_2 = \mu\left(\frac{1}{2}\left(\boldsymbol{H}^c_{AC}\otimes\boldsymbol{H}^c_{AC} - \boldsymbol{H}^s_{AC}\otimes\boldsymbol{H}^s_{AC}\right) - \frac{1}{4}\left(\boldsymbol{H}^c_{AC}\cdot\boldsymbol{H}^c_{AC} - \boldsymbol{H}^s_{AC}\cdot\boldsymbol{H}^s_{AC}\right)\boldsymbol{I}\right), \tag{14}$$

$$\boldsymbol{T}^s_2 = \mu\left(\frac{1}{2}\left(\boldsymbol{H}^c_{AC}\otimes\boldsymbol{H}^s_{AC} + \boldsymbol{H}^s_{AC}\otimes\boldsymbol{H}^c_{AC}\right) - \frac{1}{2}\left(\boldsymbol{H}^c_{AC}\cdot\boldsymbol{H}^s_{AC}\right)\boldsymbol{I}\right). \tag{15}$$

The stress tensors $\boldsymbol{T}_0$ and $\boldsymbol{T}_2$, and their associated mechanical problems, will be neglected in our formulation.

3.3.4. Output of interest

The output of interest is the dissipated (Ohmic) power as a function of the input angular frequency ω in the Z-gradient coil. If the fields can be represented as complex amplitudes, the (average) Ohmic power (or dissipated power), as a function of the drive frequency, can be computed according to [34]

$$P^o_\Omega(\omega, \boldsymbol{A}_{AC}) = \frac{1}{2}\int_\Omega \gamma^{-1}|\boldsymbol{J}^o|^2 \mathrm{d}\Omega = \frac{1}{2}\int_\Omega \gamma\,|\boldsymbol{E}_{AC}|^2 \mathrm{d}\Omega = \frac{1}{2}\int_\Omega \gamma\,|\mathrm{i}\omega\boldsymbol{A}_{AC}|^2 \mathrm{d}\Omega. \tag{16}$$

3.3.5. Fixed point algorithm

The approach presented in [8] has been reported to give a 20–100 factor reduction in computational time compared to a previous transient formulation [5] and, along similar lines, we present a fixed point algorithm for the solution of (9)–(11) in Algorithm 1.

Algorithm 1: Fixed point algorithm.

Compute $\boldsymbol{H}_{DC} = \mu_0^{-1}\nabla\times\boldsymbol{A}_{AC}$ by solving (9);
Compute $\boldsymbol{H}^{[0]}_{AC} = \boldsymbol{H}_{AC}(\boldsymbol{0}) = \mu_0^{-1}\nabla\times\boldsymbol{A}_{AC}(\boldsymbol{0})$ by solving (10);
for $k = 0, 1, 2, \cdots$ *or until convergence reached* **do**
  Compute $\boldsymbol{u}^{[k+1]} = \boldsymbol{u}(\boldsymbol{H}_{DC}, \boldsymbol{H}^{[k]}_{AC})$ by solving (11);
  Compute $\boldsymbol{H}^{[k+1]}_{AC} = \boldsymbol{H}_{AC}(\boldsymbol{u}^{[k+1]}) = \mu_0^{-1}\nabla\times\boldsymbol{A}_{AC}(\boldsymbol{u}^{[k+1]})$ by solving (10);
end

The output of interest is the (average) Ohmic power (or dissipated power) as a function of the drive frequency for the Z-gradient coil, which can be computed, for some converged iteration M, as $P^o_\Omega(\omega, \boldsymbol{A}^{[M]}_{AC})$ using (16). The stopping criteria for the fixed point algorithm is chosen to be associated with the dissipated power. Introducing the notation

$$\boldsymbol{P}^o\left(\omega, \boldsymbol{A}^{[M]}_{AC}\right) = \left(P^o_{\Omega^{4K}_c}\left(\omega, \boldsymbol{A}^{[M]}_{AC}\right) \quad P^o_{\Omega^{77K}_c}\left(\omega, \boldsymbol{A}^{[M]}_{AC}\right) \quad P^o_{\Omega^{OVC}_c}\left(\omega, \boldsymbol{A}^{[M]}_{AC}\right),\right), \tag{17}$$

for the vector of dissipated power associated with the 4K shield, 77K shield and the OVC our stopping criteria is

$$\eta^{[k]} = \frac{\|\boldsymbol{P}^o(\omega, \boldsymbol{A}^{[k+1]}_{AC}) - \boldsymbol{P}^o(\omega, \boldsymbol{A}^{[k]}_{AC})\|}{\|\boldsymbol{P}^o(\omega, \boldsymbol{A}^{[k+1]}_{AC})\|} \leq TOL. \tag{18}$$

4. Computational treatment of axisymmetric problems

Being rotationally symmetric, the aforementioned industrial problem described in Section 3 lends itself to being treated as an axisymmetric problem, which offers considerable computational advantages over its solution in three dimensions. Introducing the cylindrical coordinates (r, ϕ, z), and the unit vectors $(\boldsymbol{e}_r, \boldsymbol{e}_\phi, \boldsymbol{e}_z)$ associated with the coordinate axes, the domain becomes the r, z plane as illustrated in Fig. 3. As the currents are angular $\boldsymbol{J}^s = J^s_\phi(r,z)\boldsymbol{e}_\phi$, $\boldsymbol{J}^l = J^l_\phi(r,z)\boldsymbol{e}_\phi$ and $\boldsymbol{J}^o = J^o_\phi(r,z)\boldsymbol{e}_\phi$ then the fields for the axisymmetric problem become

$$\boldsymbol{H}(r,\phi,z) = \boldsymbol{H}(r,z) = H_r\boldsymbol{e}_r + H_z\boldsymbol{e}_z, \tag{19}$$

$$\boldsymbol{E}(r,\phi,z) = \boldsymbol{E}(r,z) = E_\phi\boldsymbol{e}_\phi, \tag{20}$$

$$\boldsymbol{A}(r,\phi,z) = \boldsymbol{A}(r,z) = A_\phi\boldsymbol{e}_\phi, \tag{21}$$

$$\boldsymbol{u}(r,\phi,z) = \boldsymbol{u}(r,z) = u_r\boldsymbol{e}_r + u_z\boldsymbol{e}_z. \tag{22}$$

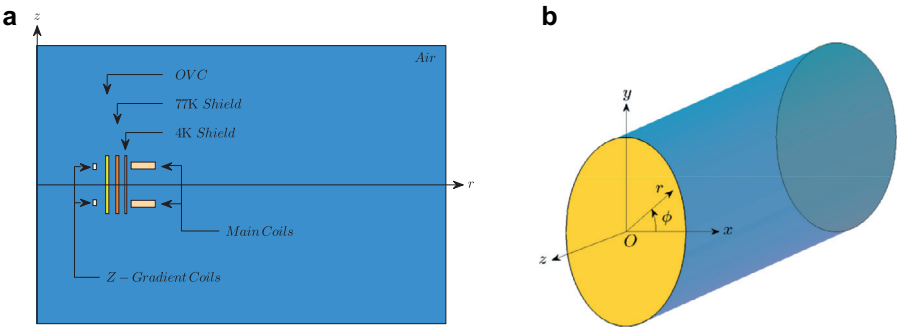

Fig. 3. Simplistic MRI scanner in an axisymmetric geometry; (a) is a longitudinal sectional cut of (b).

4.1. Weak form of the magneto-static problem (9)

Considering first the three-dimensional domain Ω_{DC}, the weak form associated with (9) is: Find $\boldsymbol{A}_{DC} \in \boldsymbol{X}_{DC}$ such that

$$\int_{\Omega_{DC}} \mu^{-1} \nabla \times \boldsymbol{A}_{DC} \cdot \nabla \times \boldsymbol{w} \, \mathrm{d}\Omega = \int_{\Omega_{DC}} \boldsymbol{J}^s_{DC} \cdot \boldsymbol{w} \, \mathrm{d}\Omega \quad \forall \boldsymbol{w} \in \boldsymbol{X}_{DC}, \tag{23}$$

where

$$\boldsymbol{X}_{DC} := \{\boldsymbol{A}_{DC} \in \boldsymbol{H}(\mathrm{curl}, \Omega_{DC}) : \nabla \cdot \boldsymbol{A}_{DC} = 0 \text{ in } \Omega_{DC}, \ \boldsymbol{n} \times \boldsymbol{A}_{DC} = \boldsymbol{0} \text{ on } \partial\Omega_{DC}\}.$$

In an axisymmetric domain, this reduces to: Find $A_{\phi DC} \in X^{\mathrm{cyl}}_{DC}$ such that

$$\int_{\Omega^p_{DC}} \mu^{-1} \left(\frac{\partial A_{\phi DC}}{\partial z} \frac{\partial w_\phi}{\partial z} + \frac{1}{r^2} \frac{\partial (r A_{\phi DC})}{\partial r} \frac{\partial (r w_\phi)}{\partial r} \right) r \, \mathrm{d}r\mathrm{d}z = \int_{\Omega^p_{DC}} J^s_{\phi DC} w_\phi r \, \mathrm{d}r\mathrm{d}z \quad \forall w_\phi \in X^{\mathrm{cyl}}_{DC}, \tag{24}$$

where Ω^p_{DC} is the rotationally symmetric (r, z) plane of Ω_{DC} and

$$X^{\mathrm{cyl}}_{DC} := \left\{ A_{\phi DC} : A_{\phi DC} \in L^2_1(\Omega^p_{DC}), \begin{pmatrix} -\frac{\partial A_{\phi DC}}{\partial z} \\ \frac{1}{r} \frac{\partial (r A_{\phi DC})}{\partial r} \end{pmatrix} \in (L^2_1(\Omega^p_{DC}))^2, \ A_{\phi DC} = 0 \text{ on } \Gamma_\infty \right\},$$

$$L^2_1(\Omega^p_{DC}) := \left\{ u : u \in L^2(\Omega^p_{DC}), \ \sqrt{r} u \in L^2(\Omega^p_{DC}) \right\},$$

are suitable weighted spaces [26], $\partial\Omega_{DC} = \Gamma_\infty \cup \Gamma_0$ and Γ_0 is the $r = 0$ axis. Note that the Coulomb gauge is automatically satisfied in this case.

With a finite element approach in mind, one could consider trying to derive suitable finite element basis functions for X^{cyl}_{DC} (e.g. in a similar way to [26]) or, alternatively, choose to treat the unbounded integrations by regularising through numerical integration [29]. However, an alternative approach, which allows standard basis functions to be used, is to introduce $A_{\phi DC} = r\hat{A}_{\phi DC}$, $w_\phi = r\hat{w}_\phi$ and the modified weak form: Find $\hat{A}_{\phi DC} \in \hat{X}^{\mathrm{cyl}}_{DC}$ such that

$$\int_{\Omega^p_{DC}} \frac{\mu^{-1}}{r} \nabla_p (r^2 \hat{A}_{\phi DC}) \cdot \nabla_p (r^2 \hat{w}_\phi) \, \mathrm{d}r\mathrm{d}z = \int_{\Omega^p_{DC}} J^s_{\phi DC} \hat{w}_\phi r^2 \, \mathrm{d}r\mathrm{d}z \quad \forall \hat{w}_\phi \in \hat{X}^{\mathrm{cyl}}_{DC}, \tag{25}$$

where $\nabla_p(\cdot)$ is the gradient operator applied in the (r, z) plane and

$$\hat{X}^{\mathrm{cyl}}_{DC} := \left\{ \hat{A}_{\phi DC} : \hat{A}_{\phi DC} \in L^2(\Omega^p_{DC}), \ \nabla_p \hat{A}_{\phi DC} \in (L^2(\Omega^p_{DC}))^2, \ \hat{A}_{\phi DC} = 0 \text{ on } \Gamma_\infty \right\}, \tag{26}$$

Note that on expansion of the terms in (25) the integrands now become well-behaved as $r \to 0$ and the solution space $\hat{X}^{\mathrm{cyl}}_{DC}$ allows standard H^1 conforming finite element discretisations to be employed. The discrete weak form is: Find $\hat{A}^{hp}_{\phi DC} \in \hat{X}^{\mathrm{cyl}}_{DC} \cap X_{hp}$ such that

$$\int_{\Omega^p_{DC}} \frac{\mu^{-1}}{r} \nabla_p (r^2 \hat{A}^{hp}_{\phi DC}) \cdot \nabla_p (r^2 \hat{w}^{hp}_\phi) \, \mathrm{d}r\mathrm{d}z = \int_{\Omega^p_{DC}} J^s_{\phi DC} \hat{w}^{hp}_\phi r^2 \, \mathrm{d}r\mathrm{d}z \tag{27}$$

for all $\forall \hat{w}^{hp}_\phi \in \hat{X}^{\mathrm{cyl}}_{DC} \cap X_{hp}$ where $X_{hp} \subset H^1(\Omega^p)$ is a suitable set of hierarchic basis functions e.g. [35].

4.2. Weak form of the quasi-static problem (10)

The computational treatment of (10), which involves setting up the weak form on the (r, z) plane of Ω, Ω^p, is analogous to that of (9) and is therefore omitted.

4.3. Weak form of the elasticity equation (11)

Considering first the three-dimensional domain Ω, the weak form associated with (11) is: Find $\boldsymbol{u} \in \boldsymbol{Y}(\boldsymbol{u}_D)$ such that

$$\int_{\Omega_c} \left((\boldsymbol{\sigma}^m(\boldsymbol{u}) + \boldsymbol{T}) : \nabla \boldsymbol{w} - \rho\omega^2 \boldsymbol{u} \cdot \boldsymbol{w} \right) \mathrm{d}\Omega = \int_{\Gamma_c^N} \boldsymbol{t} \cdot \boldsymbol{w} \, \mathrm{d}s \quad \forall \boldsymbol{w} \in \boldsymbol{Y}(\boldsymbol{0}), \tag{28}$$

where

$$\boldsymbol{Y}(\boldsymbol{u}_D) := \left\{ \boldsymbol{u} \in (H^1(\Omega_c))^3 : \boldsymbol{u} = \boldsymbol{u}_D \text{ on } \Gamma_c^D \right\}.$$

In cylindrical coordinates the linearised strain tensor for $\boldsymbol{u} = u_r \boldsymbol{e}_r + u_z \boldsymbol{e}_z$ becomes

$$\boldsymbol{\varepsilon} = \begin{bmatrix} \varepsilon_{rr} & \varepsilon_{r\phi} & \varepsilon_{rz} \\ \varepsilon_{\phi r} & \varepsilon_{\phi\phi} & \varepsilon_{\phi z} \\ \varepsilon_{zr} & \varepsilon_{z\phi} & \varepsilon_{zz} \end{bmatrix} = \begin{bmatrix} \dfrac{\partial u_r}{\partial r} & 0 & \dfrac{1}{2}\left(\dfrac{\partial u_r}{\partial z} + \dfrac{\partial u_z}{\partial r} \right) \\ 0 & \dfrac{u_r}{r} & 0 \\ \dfrac{1}{2}\left(\dfrac{\partial u_r}{\partial z} + \dfrac{\partial u_z}{\partial r} \right) & 0 & \dfrac{\partial u_z}{\partial z} \end{bmatrix},$$

which is also the form quoted by Zienkiewicz [30] as well as Timoshenko and Goodier [36]. By following a similar approach to that outlined in Section 4.1 and introducing the new displacement field and weight as

$$\tilde{\boldsymbol{u}} := r\hat{u}_r \boldsymbol{e}_r + u_z \boldsymbol{e}_z, \quad \tilde{\boldsymbol{w}} := r\hat{w}_r \boldsymbol{e}_r + w_z \boldsymbol{e}_z,$$

and also defining

$$\hat{\boldsymbol{u}} := \hat{u}_r \boldsymbol{e}_r + u_z \boldsymbol{e}_z, \quad \hat{\boldsymbol{w}} := \hat{w}_r \boldsymbol{e}_r + w_z \boldsymbol{e}_z,$$

it is possible to show that the weak form becomes: Find $\hat{\boldsymbol{u}} \in \hat{\boldsymbol{Y}}^{\mathrm{cyl}}(\hat{\boldsymbol{u}}_D)$ such that

$$\begin{aligned} &\int_{\Omega_c^p} (\lambda \nabla \cdot \tilde{\boldsymbol{u}} \, \nabla \cdot \tilde{\boldsymbol{w}} + 2G \nabla^s \tilde{\boldsymbol{u}} : \nabla^s \tilde{\boldsymbol{w}} - \rho\omega_m^2 \tilde{\boldsymbol{u}} \cdot \tilde{\boldsymbol{w}}) r \, \mathrm{d}r\mathrm{d}z \\ &\quad = -\int_{\Omega_c^p} \boldsymbol{T} : \nabla^s \tilde{\boldsymbol{w}} r \, \mathrm{d}r\mathrm{d}z + \int_{\Gamma_c^{Np}} \tilde{\boldsymbol{w}} \cdot ((\boldsymbol{\sigma}^m(\boldsymbol{u}) + \boldsymbol{T})\boldsymbol{n}) r \, \mathrm{d}s \; \forall \, \tilde{\boldsymbol{w}} \in \hat{\boldsymbol{Y}}^{\mathrm{cyl}}(\boldsymbol{0}), \end{aligned} \tag{29}$$

where Ω_c^p is the rotationally symmetric (r, z) plane of Ω_c, $\partial\Omega_c^p = \Gamma_c^{Dp} \cup \Gamma_c^{Np}$, note there is no $r = 0$ component to $\partial\Omega_c^p$ as we have chosen our conducting components to be placed away from this axis. Also note that

$$\hat{\boldsymbol{Y}}^{\mathrm{cyl}}(\hat{\boldsymbol{u}}_D) := \left\{ \hat{\boldsymbol{u}} : \hat{\boldsymbol{u}} \in \left(H^1(\Omega_c^p)^2 \right), \; \hat{\boldsymbol{u}} = \hat{\boldsymbol{u}}_D \text{ on } \Gamma_c^{Dp} \right\},$$

and in cylindrical coordinates

$$\begin{aligned} \nabla \cdot \tilde{\boldsymbol{u}} &= \frac{1}{r}\frac{\partial (r^2 \hat{u}_r)}{\partial r} + \frac{\partial u_z}{\partial z} = \frac{\partial (r\hat{u}_r)}{\partial r} + \frac{(r\hat{u}_r)}{r} + \frac{\partial u_z}{\partial z}, \\ \nabla^s \tilde{\boldsymbol{u}} &= \frac{\partial (r\hat{u}_r)}{\partial r} \boldsymbol{e_r} \otimes \boldsymbol{e_r} + \frac{(r\hat{u}_r)}{r} \boldsymbol{e_\phi} \otimes \boldsymbol{e_\phi} + \frac{\partial u_z}{\partial z} \boldsymbol{e_z} \otimes \boldsymbol{e_z} \\ &\quad + \frac{1}{2}\left(\frac{\partial (r\hat{u}_r)}{\partial z} + \frac{\partial u_z}{\partial r} \right) \boldsymbol{e_r} \otimes \boldsymbol{e_z} + \frac{1}{2}\left(\frac{\partial (r\hat{u}_r)}{\partial z} + \frac{\partial u_z}{\partial r} \right) \boldsymbol{e_z} \otimes \boldsymbol{e_r}. \end{aligned}$$

As previously, on expansion of the terms the integrands in (29) remain well behaved as $r \to 0$ and the solution space $\hat{\boldsymbol{Y}}^{\mathrm{cyl}}(\hat{\boldsymbol{u}}_D)$ allows standard H^1 conforming finite elements discretisations to be employed. The corresponding discrete weak form is: Find $\hat{\boldsymbol{u}}^{hp} \in \hat{\boldsymbol{Y}}^{\mathrm{cyl}}(\hat{\boldsymbol{u}}_D) \cap \boldsymbol{Y}_{hp}$ such that

$$\begin{aligned} &\int_{\Omega_c^p} (\lambda \nabla \cdot \tilde{\boldsymbol{u}}^{hp} \, \nabla \cdot \tilde{\boldsymbol{w}}^{hp} + 2G \nabla^s \tilde{\boldsymbol{u}}^{hp} : \nabla^s \tilde{\boldsymbol{w}}^{hp} - \rho\omega_m^2 \tilde{\boldsymbol{u}}^{hp} \cdot \tilde{\boldsymbol{w}}^{hp}) r \, \mathrm{d}r\mathrm{d}z \\ &\quad = -\int_{\Omega_c^p} \boldsymbol{T} : \nabla^s \tilde{\boldsymbol{w}}^{hp} r \, \mathrm{d}r\mathrm{d}z + \int_{\Gamma_c^{Np}} \tilde{\boldsymbol{w}}^{hp} \cdot ((\boldsymbol{\sigma}^m(\boldsymbol{u}) + \boldsymbol{T})\boldsymbol{n}) r \, \mathrm{d}s \end{aligned} \tag{30}$$

for all $\hat{\boldsymbol{w}}^{hp} \in \hat{\boldsymbol{Y}}^{\mathrm{cyl}}(\boldsymbol{0}) \cap \boldsymbol{Y}_{hp}$ where $\boldsymbol{Y}_{hp} := \{\hat{\boldsymbol{u}} : \hat{u}_r \in X_{hp}, \hat{\boldsymbol{u}}_z \in X_{hp}\}$.

5. Numerical results

As an illustration of the numerical results for this problem, we consider an application of p-refinement on a finite element mesh consisting of 6820 unstructured triangular elements which represents the complete configuration, including the main coils, the Z-gradient coils, the 4K and 77K shields as well as the OVC. The mesh density has been chosen so that the features of

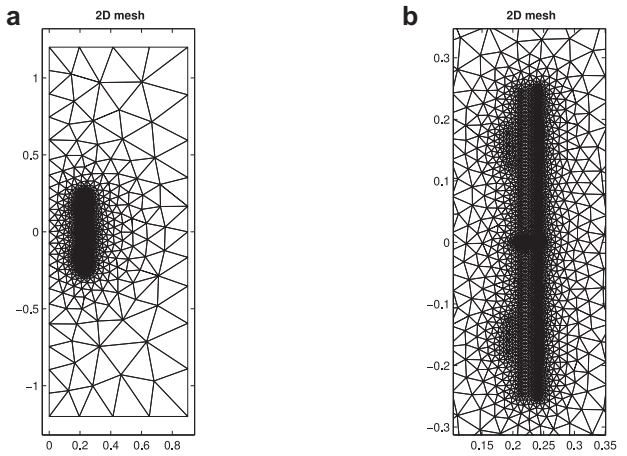

Fig. 4. (a) Mesh of 6820 unstructured triangular elements for Ω^p for the eddy current problem and (b) a close-up showing the details of the coils, shields, and OVC.

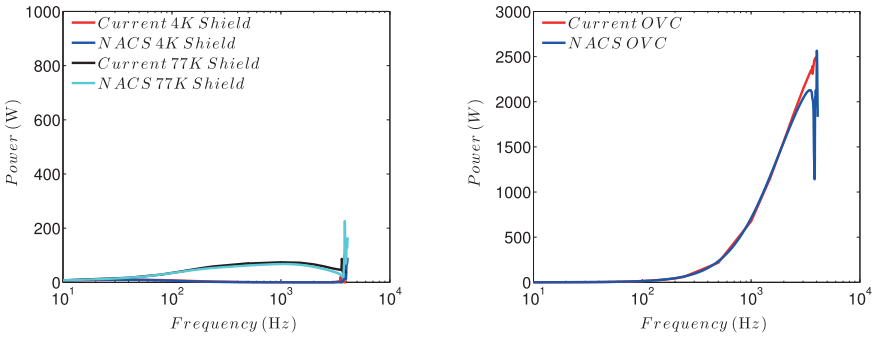

Fig. 5. Comparison of the Ohmic power in the 4K shield, 77K shield, and OVC obtained using our fixed point algorithm using a discretisation with uniform $p = 1$ elements and that obtained with NACS.

the problem, including edges and sharp corners are well described. Results obtained on other meshes of similar construction are in close agreement. The complete configuration for the (r, z) plane of Ω, namely Ω^p is shown in Fig. 4. In addition, the region corresponding to the key conducting components, namely the shields and OVC, can be better identified in the zoom of the central region. These subdomains make up Ω_c^p in which the mechanical problem is to be solved.

We consider elements of order $p = 1, 2, 3, 4, 5$, in turn, and apply these throughout the domains Ω^p and Ω_c^p, on the aforementioned meshes, to discretise the problem with one exception: Due to the high degree of nonlinearity of $\boldsymbol{\sigma}^e \boldsymbol{n}|_{\partial\Omega^c}$, we perform under integration of this term by restricting its evaluation to using $p = 1$ elements. We then apply the fixed point algorithm described in Section 3.3 where we set the tolerance for the convergence criteria established in (18) as $\mathrm{TOL} = 10^{-2}$. We perform a sweep through frequencies ranging from $f = \omega/(2\pi) = 10$ Hz to $f = 4200$ Hz and consider the Ohmic power $P^o_{\Omega_c^{4K}}(\omega)$, $P^o_{\Omega_c^{77K}}(\omega)$, $P^o_{\Omega_c^{OVC}}(\omega)$ obtained in the 4K and 77K shields as well as the OVC as a function of frequency. The results of this investigation are shown in Figs. 5–9 for $p = 1, 2, 3, 4, 5$, respectively. In each of these figures, we also make comparisons with the results obtained from the commercial NACS software [12] developed by SIMetris GmbH using low order $p = 1$ elements and a mesh of 7857 elements. For the case of $p = 5$ we also include the results for the uncoupled problem, in which the right hand side in equation (10a) is set to zero. As p is increased the results of simulations converge and exhibit similarities to those obtained with NACS. Moreover, for low frequencies, the Lorentz force is negligible and the Ohmic power is essentially identical to that obtained from solving the eddy current problem for the Z-gradient coils (10) with the right hand side in (10a) set to zero, as illustrated in the results for $p = 5$ elements. However, at higher frequencies (above 3 KHz), the Lorentz force increases and the effects of the coupling between electromagnetic problem(s) and the mechanical problems become stronger. In particular, in order to properly understand the behaviour of the fields in this region, an accurate discretisation is required particularly in the frequency range 3–4 KHz, which is also known to be associated with the free vibration resonant frequencies of the screens and OVC if treated as thin cylindrical shells [37] (see equation (2.26)). We observe that for lower frequencies, using $p = 1$ is already sufficient to generate good agreement with the NACS software, however, for higher frequencies, elements with $p \geq 4$ are required to achieve mesh/discretisation convergence. This is particularly evident close to the resonance region. It is worth remarking that the peak values in $P^o_{\Omega_c^{4K}}(\omega)$, $P^o_{\Omega_c^{77K}}(\omega)$ at resonance are larger than those obtained by NACS and this is in part due to the additional

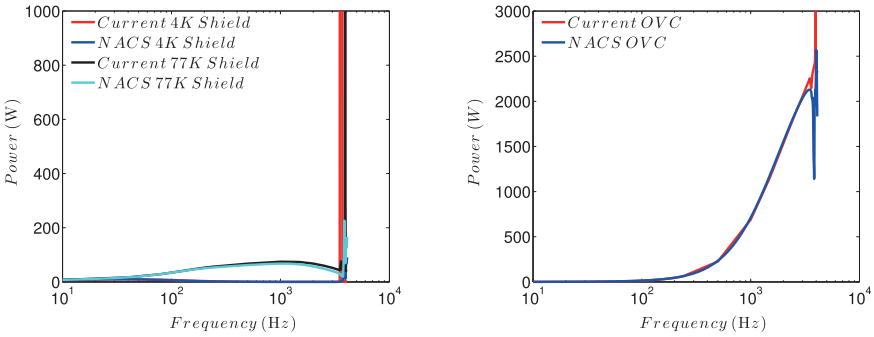

Fig. 6. As Fig. 5 but with uniform $p = 2$ elements.

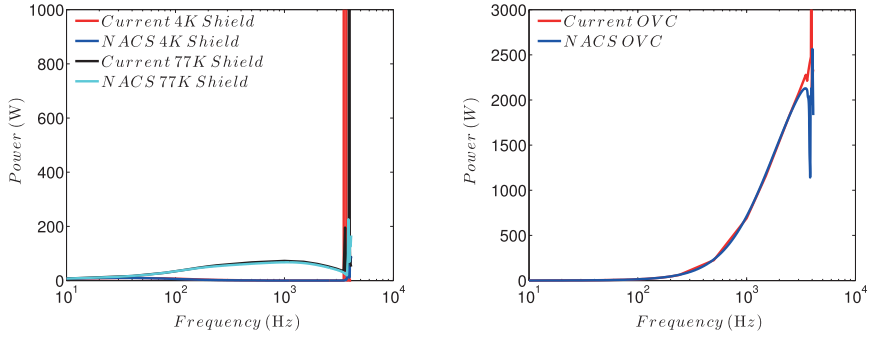

Fig. 7. As Fig. 5 but with uniform $p = 3$ elements.

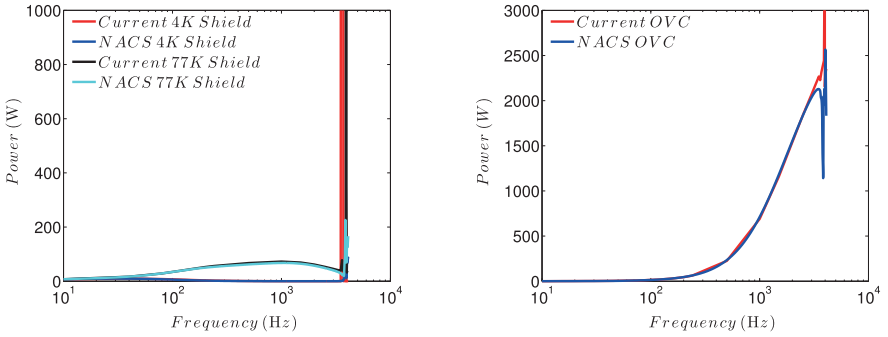

Fig. 8. As Fig. 5 but with uniform $p = 4$ elements.

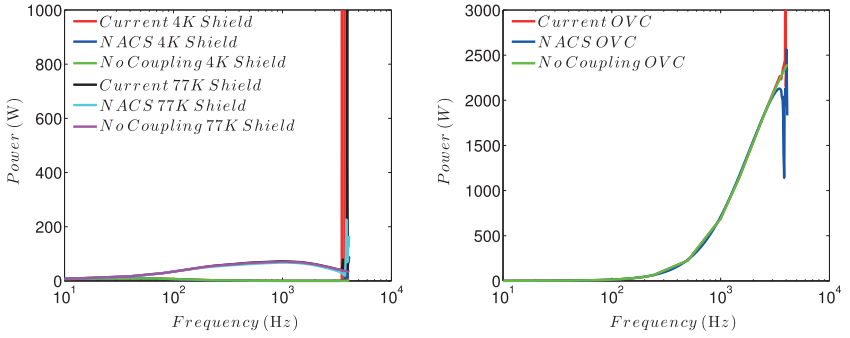

Fig. 9. As Fig. 5 but with uniform $p = 5$ elements.

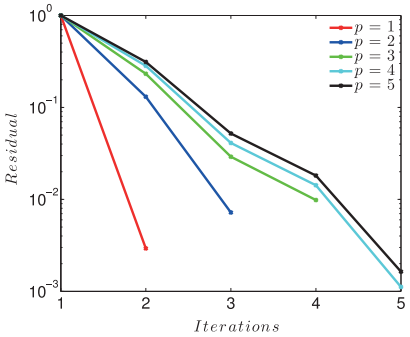

Fig. 10. Convergence of the fixed-point iteration for the frequency of 3925 Hz in the resonance region for discretisations consisting of uniform $p = 1, 2, 3, 4, 5$ elements.

numerical dissipation added by the NACS software. At resonance, we expect the Ohmic power to tend towards infinity in the absence of numerical dissipation.

The number of iterations required to reach convergence depends on the frequency. Away from the resonance region, 2–3 iterations or less are typically sufficient in order to ensure convergence of the scheme. However, close to the resonance region, the number of iterations required to reach the desired tolerance can increase. In Fig. 10, we show the convergence of $\eta^{[k]}$ for the frequency of 3925Hz in the resonance region. As our primary concern in this work is to deliver high levels of numerical accuracy, we have chosen not to present computational timings. Moreover, we believe that a significant computational gain could be obtained by implementation of our computational approach in an alternative language such as Fortran and utilising parallel processing for the trivially parallelisable frequency sweep rather than the serial vectorised MATLAB [38] implementation used here. This will be part of our future work.

In order to explain the need for higher fidelity discretisations as the frequency increases one should consider the skin depth $\delta := \sqrt{2/(\omega\mu_0\gamma)}$ [32]. Recall that the skin depth measures the depth to which the current density has fallen to $1/e$ of its surface value and that at higher frequencies smaller skin depths are to be expected [25]. Then, in order to resolve the sharp field gradients that occur in the layer close to the surface of the conductor, finer fidelity of the discretisation is required. For example, at frequency of $f = 4100$Hz, the skin depth is $O(10^{-4})$m, which is approximately one-tenth of the width of the shields.

6. Concluding remarks

This paper has presented a fixed point algorithm for the solution of magneto–mechanical coupling associated with generation of Lorentz forces in axisymmetric conductors as a result of eddy currents generated by low frequency magnetic fields. The solution strategy is based on computing these forces using a stress tensor approach and new weak variational statements have been developed that can be discretised by the *hp*-version of H^1 conforming finite elements without the need to regularise singular integrals by numerical integration. The approach has been applied to a benchmark problem proposed by Siemens plc where the importance of using high order elements for accurately predicting the eddy currents and the associated coupling in the resonance region has been illustrated.

Acknowledgements

The financial support received in the form of a CASE award Ph.D. studentship from EPSRC (Engineering and Physical Sciences Research Council, UK) and Siemens is gratefully acknowledged. The first author would like to acknowledge the financial support received through the EPSRC grant EP/K023950/1 and the second author through “The Leverhulme Prize” awarded by The Leverhulme Trust, UK.

References

[1] S.C. Atlas (Ed.), Magnetic Resonance Imaging of the Brain and Spine, vol. 1, Lippincott Williams and Wilkins, 2009.
[2] M. Kaltenbacher, H. Landes, R. Lerch, An efficient calculation scheme for the numerical simulation of coupled magnetomechanical systems, IEEE Trans. Magnet. 33 (1997) 1646–1649.
[3] M. Schinnerl, J. Schöberl, M. Kaltenbacher, R. Lerch, Multigrid methods for the simulation of nonlinear magnetomechanical systems, IEEE Trans. Magnet. 38 (2002) 1497–1511.
[4] A. Krug, M. Rausch, P. Dietz, H. Landes, M. Kaltenbacher, W. Rathmann, F. Vogel, Slides presented at Numerical modelling and design optimisation of clinical MRI scanners, in: 23rd CADFEM User's Meeting, 2005.
[5] M. Rausch, M. Gebhardt, M. Kaltenbacher, H. Landes, Magnetomechanical field computations of a clinical magnetic resonance imaging (MRI) scanner, COMPEL 22 (3) (2003) 576–588.
[6] M. Rausch, M. Gebhardt, M. Kaltenbacher, H. Landes, Computer-aided design of clinical magnetic resonance imaging scanners by coupled magnetomechanical–acoustic modeling, IEEE Trans. Magnet. 41 (2005) 72–81.
[7] M. Schinnerl, M. Kaltenbacher, U. Langer, R. Lerch, J. Schöberl, An efficient method for the numerical simulation of magneto-mechanical sensors and actuators, Eur. J. Appl. Math. 18 (2007) 233–271.

[8] A. Krug, H. Landes, A. Stein, P. Dietz, Slides presented at Modal analysis for coupled magneto-mechanical systems applied to MRI scanners, in: ANSYS Conference and 30th CADFEM Users Meeting, 2012.
[9] H. Landes, P. Dietz, A. Krug, A. Stein, Slides presented at Simulations in ultra-high-field magnetic resonance imaging, in: ANSYS Conference and 28th CADFEM Users Meeting, 2010.
[10] ANSYS, UK, http://www.ansys.com (accessed 24.04.15).
[11] COMSOL multiphysics software, http://www.uk.comsol.com/ (accessed 28.07.14).
[12] SIMetris GmbH, Numerical analysis of coupled systems (NACS), http://www.simetris.de (accessed 28.07.14).
[13] Z. Ren, Comparison of different force calculation methods in 3D finite element modelling, IEEE Trans. Magnet. 30 (1994) 3471–3474.
[14] A.J. Gil, A. Arranz Carreño, J. Bonet, O. Hassan, The immersed structural potential method for haemodynamic applications, J. Comput. Phys. 229 (2010) 8613–8641.
[15] C. Hesch, A.J. Gil, A. Arranz Carreño, J. Bonet, On continuum immersed strategies for fluid-structure interaction, Comput. Methods Appl. Mech. Eng. 247 (2012) 51–64.
[16] A.J. Gil, A. Arranz Carreño, J. Bonet, O. Hassan, An enhanced immersed structural potential method for fluid-structure interaction, J. Comput. Phys. 250 (2013) 178–205.
[17] M. Kaltenbacher, Numerical Simulation of Mechatronic Sensors and Actuators, Springer, Heidelberg, 2007.
[18] A.J. Gil, P.D. Ledger, A coupled *hp*-finite element scheme for the solution of two-dimensional electrostrictive materials, Int. J. Numer. Method. Eng. 91 (11) (2012) 1158–1183.
[19] D. Jin, P.D. Ledger, A.J. Gil, An hp-fem framework for the simulation of electrostrictive and magnetostrictive materials, Comput. Struct. 133 (2014) 131–148.
[20] J.A. Adams, Electromagnetic Theory, John Wiley & Sons, 2007.
[21] A.C. Eringen, G.A. Maugin, Electrodynamics of Continua I: Foundations and Solid Media, Springer, Heidelberg, 2011.
[22] L. Demkowicz, Computing with *hp*-Adaptive Finite Elements: Vol. 1: One and Two Dimensional Elliptic and Maxwell Problems, Chapman and Hall, Boca Raton FL, USA, 2007.
[23] L. Demkowicz, J. Kurtz, D. Pardo, M. Paszynski, W. Rachowicz, A. Zdunek, Computing with *hp*-Adaptive Finite Elements: Vol. 2: Frontiers: Three Dimensional Elliptic and Maxwell Problems with Applications, Chapman and Hall, Boca Raton FL, USA, 2007.
[24] I. Gomez-Revuelto, L.E. Garcia-Castillo, D. Pardo, L. Demkowicz, A two-dimensional self-adaptive *hp* finite element method for the analysis of open region problems in electromagnetics, IEEE Trans. Magnet. 43 (2007) 1337–1340.
[25] P.D. Ledger, S. Zaglmayr, *hp*-finite element simulation of three-dimensional eddy current problems on multiply connected domains, Comput. Method Appl. Mech. Eng. 199 (49–52) (2010) 3386–3401.
[26] P. Lacoste, Solution of Maxwell equation in axisymmetric geometry by Fourier series decomposition and by use of H(rot) conforming finite element, Numer. Math. 84 (4) (2000) 577–609.
[27] V.M. Machado, Axisymmetric eddy current problems using a special hybrid fe/be method, IEEE Trans. Magnet. 39 (2003) 1143–1146.
[28] V.M. Machado, J.F.B. de Silva, Magnetic forces for axisymmetric eddy current problems using a hybrid fe/be method, IEEE Trans. Magnet. 42 (2006) 1463–1466.
[29] R. Hiptmair, P.D. Ledger, Computation of resonant modes for axisymmetric Maxwell cavities using *hp*-version edge finite elements, Int. J. Numer. Method Eng. 62 (12) (2005) 1652–1676.
[30] O.C. Zienkiewicz, The Finite Element Method in Engineering Science, second, McGraw-Hill Inc., Berkshire, England, 1971.
[31] M. Kruip, Siemens plc benchmark problem, 2013, personal communication.
[32] A. Bossavit, Computational Electromagnetism: Variational Formulations, Complementarity, Edge Elements, first, Academic Press, San Diego, USA, 1998.
[33] H. Ammari, A. Buffa, J.C. Nédélec, A justification of eddy currents model for the Maxwell equations, SIAM J. Appl. Math. 60 (2000) 1805–1823.
[34] W.R. Smythe, Static and Dynamic Electricity, third, Taylor & Francis, Bristol, England, 1989.
[35] J. Schöberl, S. Zaglmayr, High order Nédélec elements with local complete sequence properties, Int. J. Comput. Math. Electr. Electron. Eng. (COMPEL) 24 (2) (2005) 374–384.
[36] S. Timoshenko, J.N. Goodier, Theory of Elasticity, second, McGraw-Hill Inc., New York, 1951.
[37] A. Leissa, Vibration of Shells, Technical Report, 1973.NASA SP-288
[38] MathWorks, MATLAB, http://uk.mathworks.com (accessed 28.07.14).